CHEMISTRY OF MATERIALS

pubs.acs.org/cm

Article

Unveiling Stability Factors in Sn(II)-Containing Oxides: Discovery of a Polar Tin Titanate and Photocatalytic Activity for Overall Water Splitting

Eric A. Gabilondo, Shaun O'Donnell, Subhendu Jana, Rachel Broughton, Mingli Liang, Aylin Koldemir, Jack Reichling, Carson Campbell, P. Shiv Halasyamani, Rainer Pöttgen, Jacob L. Jones, and Paul A. Maggard*

Cite This: *Chem. Mater.* 2024, 36, 5753−5763

Read Online

ACCESS | Metrics & More | Article Recommendations | Supporting Information

Downloaded via BAYLOR UNIV on January 10, 2025 at 18:58:45 (UTC).
See https://pubs.acs.org/sharingguidelines for options on how to legitimately share published articles.

ABSTRACT: The discovery of Sn(II)-containing oxide semiconductors has been severely limited by a lack of understanding of the factors leading to their thermodynamic stability, e.g., chemical compositions and structure types, as well as by the absence of productive synthetic routes. The relatively few reported Sn(II)−O−M (M = early transition-metal cation) semiconductors frequently decompose at moderate to low temperatures. Herein, a large-scale predictive modeling approach was used to assess the structural factors yielding their enhanced thermodynamic stability. This has resulted in 10 new predicted Sn(II)-containing oxides that are proposed to fall within reasonable synthetic limits. Increasing stability was found for structures possessing lower Sn(II)/M ratios and local asymmetric coordination environments allowing the expression of the Sn(II) stereoactive lone pair. As a test of these results, synthetic efforts to prepare one of the proposed compounds starting from $BaLa_4Ti_4O_{15}$ yielded the predicted layered-perovskite $SnLa_4Ti_4O_{15}$ (SLTO). The new SLTO crystallizes in the noncentrosymmetric and polar *P*3*c*1 space group (no. 158) as confirmed by Rietveld refinements of powder X-ray diffraction (XRD) data and second harmonic generation activity. Full Sn(II) substitution was confirmed by a combination of XRD structural refinements, ^{119}Sn Mössbauer spectroscopy, SEM-EDS, and X-ray photoelectron spectroscopy. UV−vis diffuse reflectance data confirmed that SLTO has a visible-light absorbing band gap of ∼2.4 eV and is a promising photocatalyst for solar energy conversion. After loading its surfaces with a $Rh/Cr_2O_3−CoO_x$ dual-cocatalyst, SLTO with hexagonal plate-shaped morphologies showed activity for overall water splitting at a rate of ∼317 μmol g^{-1} h^{-1} H_2 and an apparent quantum yield of ∼22%. Thus, these results highlight the synergistic combination of chemical intuition, predictive modeling, and synthetic design in the synthesis of new Sn(II)-containing semiconductors for promising applications of their optical properties and photocatalytic activities for water splitting.

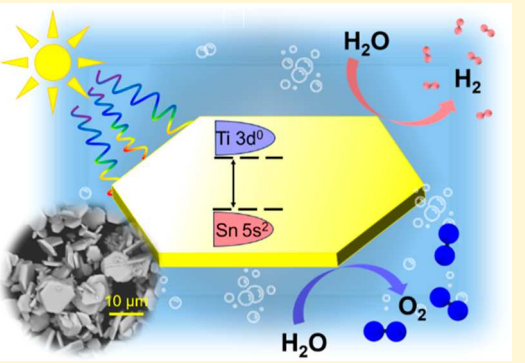

1. INTRODUCTION

Semiconducting Sn(II)-containing oxides (i.e., Sn−O−M; M = early transition-metal cation) have been identified to be promising candidates for outperforming commercial Pb(II)-containing ferroelectrics, such as in tin titanate ($SnTiO_3$ or STO) versus lead titanate ($PbTiO_3$ or PTO) perovskites, and possessing a reduced toxicity.[1,2] Additionally, many layered Sn(II)-oxides have been calculated to be potentially ideal for overall water splitting (OWS) with small optical band gaps and nearly ideal band-edge energies for solar energy conversion.[3,4] Early experimental studies of the few known Sn(II)-niobates and Sn(II)-titanates have been consistent with these predictions and have demonstrated much promise.[5,6] However, further experimental progress on this frontier has been severely limited by the synthesizability and discovery of new Sn(II)-containing oxides owing to their well-known issues of thermodynamic stability.[7−10]

The tetragonal perovskite STO is an intensely studied and predicted "holy grail" of lead-free dielectrics but has yet to be successfully synthesized.[11] A predominant reason is that STO is calculated to be unstable with respect to ilmenite-structured $SnTiO_3$, Sn_2TiO_4, and the binary oxides SnO and TiO_2. Furthermore, Sn(II) oxides are prone to oxidation in air or water to Sn(IV)-species such as cassiterite SnO_2 or rutile-type $(Ti_{1-x}Sn_x)O_2$. Given these challenges, the layered $SnTiO_3$ with the ilmenite structure type and Sn_2TiO_4 have been the only phases reported in the Sn(II)−Ti−O phase diagram.[12,13] Both

Received: March 28, 2024
Revised: May 4, 2024
Accepted: May 6, 2024
Published: May 20, 2024

© 2024 American Chemical Society

https://doi.org/10.1021/acs.chemmater.4c00929
Chem. Mater. 2024, 36, 5753−5763

compounds have been discovered only recently, with no successful reports of a perovskite-type STO due to these associated synthetic challenges. Recent reports have demonstrated the powerful utility of soft chemical, ion-exchange methods in the syntheses of new Sn(II)-containing hafnate and zirconate perovskites (i.e., $SnMO_3$).[9,10,14,15] The underlying factors governing stability and synthesizability have been hypothesized as follows: (1) kinetic stability is enhanced with (a) increased lattice energies of the substructure (i.e., MO_6 extended network), and (b) the absence of lower energy polymorphs accessible by ion diffusion, and (2) thermodynamic stability is increased with the coordination of the Sn(II) cation in asymmetric coordination environments. These hypotheses, however, require significantly more investigation in wider theoretical and experimental studies, such as to enable a deeper understanding of the structural factors leading to the stability and synthesizability of Sn(II)-containing oxides.

The emergence of machine learning tools have added an unparalleled level of high-performance data mining that can provide wider-level insights into the successful synthesis of new materials.[16,17] The frequent lack of specificity and efficient experimental validation are current bottlenecks preventing these tools from reaching broader use in discovery-driven efforts, i.e., limitations imposed by the quality and quantity of experimental training data.[18−20] Thus, these developing methods have yet to confidently predict the synthesizability of new compounds.[21] For example, a recently synthesized metastable oxide, $SnHfO_3$,[15] is predicted by one machine-learning model to be stable versus Sn, Hf, and O_2.[21] Alternative models supported by experiments show that it is unstable versus SnO and HfO_2, or SnO_2 and HfO_2, into which it rapidly decomposes when annealed under different atmospheres.[15] The aim of the current study is to effectively leverage the utility of chemically informed computational approaches to discover new, synthesizable, and Sn(II)-containing multinary oxides. Results of the electronic-structure calculations suggest stability factors and a shortlist of synthetic targets expected to be both kinetically and/or thermodynamically stable. As a test of these computational results, trial synthetic experiments of one example, $SnLa_4Ti_4O_{15}$ (SLTO), demonstrate that it can be successfully synthesized using a rapid and low temperature ion-exchange reaction with a noncentrosymmetric and polar crystal structure. Furthermore, it is found to be a promising new photocatalyst for achieving OWS under visible-light irradiation. Thus, SLTO represents the first example of the rational synthetic design of a Sn(II)-containing oxide with a polar structure, and also demonstrates an effective pathway to accelerated progress in the development of visible-light photocatalysts.

2. EXPERIMENTAL METHODS

2.1. Structure Modeling and Total Energy Calculations. A candidate set of hypothetical Sn(II)-containing oxides was constructed using the isoelectronic substitution for A-site cations, e.g., with Sn(II) replacing the Sr(II), Ba(II), or Pb(II) cations within the structures of experimentally reported multinary oxides obtained from the International Crystal Structure Database.[22] All structural modeling was performed using the visualization for electronic and structural analysis software package.[23] Elemental constituents known to be potentially redox reactive with the Sn(II) oxidation state, e.g., Mo(VI), Re(VII), and Mn(IV), were excluded from this computational data set. These criteria resulted in a list of 52 theoretical metal oxides and associated decomposition pathways, listed in Table S1 in the Supporting Information. These modeled Sn(II)-containing structures were initially geometry-relaxed using the Vienna ab initio simulation package (VASP; ver. 5.6),[24,25] within energy and ionic convergence criteria set to 1×10^{-6} eV and 0.01 eV $Å^{-1}$. For each model, Perdew−Burke−Ernzerhof functionals were used with the generalized gradients approximation using the projector augmented wave method with van der Waals corrections and Γ-centered Monkhorst−Pack grids to automatically sample the Brillouin zone.[26] Next, total energy calculations were performed for each compound with a quadrupling or more of the total number of sampled *k*-points and the energy convergence criterion increased to 1×10^{-8} eV. Using previously established methodologies.[9,14] the relative thermodynamic stability of each was determined by comparing the total energies at 0 K versus the convex hull comprised of the local phase diagram. Prior studies on ternary oxides have demonstrated an approximate computational accuracy within a standard deviation of ∼24 meV/atom with respect to decomposition reactions to the more stable binary and ternary compounds. For example, the decomposition of the cubic perovskite $SnHfO_3$ can be estimated by eqs 1 and 2.

$$SnHfO_3 \rightarrow SnO + HfO_2 \quad (1)$$

$$\Delta E_{rxn} = [\Delta E_f(SnO) + \Delta E_f(HfO_2)] - \Delta E_f(SnHfO_3) \quad (2)$$

where eq 1 is an example decomposition reaction into the binary oxides and eq 2 is the calculated relative stability.

The total densities-of-states (DOS) and band structure was calculated for the geometry relaxed $SnLa_4Ti_4O_{15}$ structure in its polar space group *P*3*c*1 (no. 158) with an energy convergence criterion set to 1×10^{-8} eV for all calculations. For the DOS, a Γ-centered 8 × 8 × 2 mesh was used with 20 *k*-points. The band structure calculations were performed next along the standard *k*-point path for its trigonal crystal system of Γ−M−K−Γ−A−L−H−A|L−M|H−K in the Brillouin zone. This calculation was performed with 10 intersecting *k*-points for each direction, representing a total of 90 *k*-points. Individual atomic orbital contributions were projected out within both the DOS and band structure plots.

2.2. Synthesis of $SnLa_4Ti_4O_{15}$. The $BaLa_4Ti_4O_{15}$ precursor was first synthesized using a molten-salt reaction within $BaBr_2$. In this step, $BaCO_3$ (Alfa Aesar, 99.8%), TiO_2 (Aldrich, 99.7%), and La_2O_3 (Alfa Aesar, 99.99%) were ground together in a 1:4:2 molar ratio with an agate mortar and pestle until thoroughly mixed. Seven molar equivalents of $BaBr_2$ (Thermo Scientific, 99%, anhydrous) were then added and ground into the mixture, i.e., (1:1 reactants to flux). The mixture was loaded into a covered alumina crucible and annealed in a box furnace in air at 1200 °C for 8 h before radiative cooling. The white crystalline powder product was washed in 250 mL of DI water then dried at 80 °C. Several representative crystals were separated from the mixture for single-crystal X-ray diffraction (XRD) characterization. The product was then finely ground prior to use in the subsequent Sn(II)-exchange reactions. A typical reaction ranged from 1 to 5 g total mass with a resultant yield of ∼90 wt % with respect to $BaLa_4Ti_4O_{15}$. To be noted, the high temperature reaction within $BaBr_2$ generates bromine gas and should be conducted in a fume hood.

In the next step, the new $SnLa_4Ti_4O_{15}$ was prepared through a cation-exchange method adapted from previous reports.[9,14] First, $SnCl_2$ (Alfa Aesar, 99%, anhydrous) and SnF_2 (Alfa Aesar, 97.5%, Alfa Aesar) in a 1:1 molar ratio were thoroughly ground with an agate mortar and pestle in an Ar glovebox to form anhydrous SnClF. Then, $BaLa_4Ti_4O_{15}$ and SnClF were mixed at a molar ratio of 1:1.5, and ground until uniform. This mixture was loaded into an evacuated fused silica ampule and flame-sealed, before annealing in a box furnace at 300 °C for 1 h and allowing the furnace to radiatively cool. The obtained product was a yellow powder that was isolated by washing by vacuum filtration with ∼350 mL of DI water followed by ∼50 mL of ethanol prior to drying at 60 °C overnight. In a typical reaction, 1.219 g (1.08 mmol) of $BaLa_4Ti_4O_{15}$ was reacted with a mixture of 0.154 g (0.81 mmol) of $SnCl_2$ and 0.127 g (0.81 mmol) of SnF_2, and the product mass recovered was ∼1.18 g after washing. The product was used, as is, for subsequent characterization and photocatalysis testing.

https://doi.org/10.1021/acs.chemmater.4c00929
Chem. Mater. 2024, 36, 5753−5763

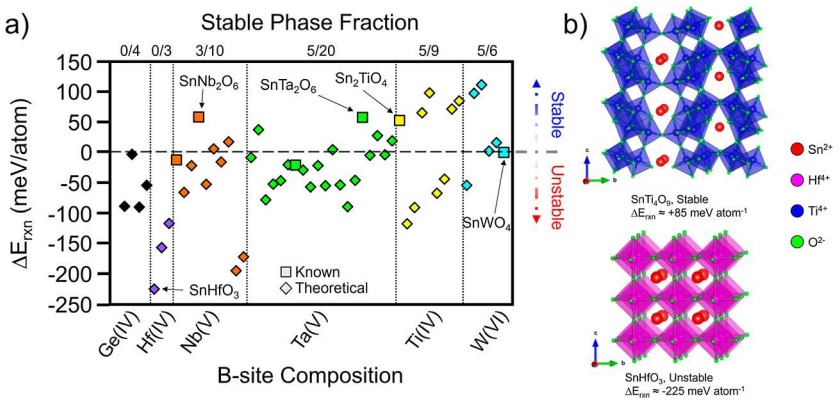

Figure 1. (a) Overview plot of calculated thermodynamic stability of the 52 hypothetical Sn(II)-containing oxides versus transition-metal cations and a main group cation. As representative examples, polyhedral drawings of (b) stable and unstable crystal structures of $SnTi_4O_9$ and $SnHfO_3$. Of the 52 modeled Sn(II)-containing oxides, 18 were calculated to be stable versus constituent binary and ternary oxides. Of these, 8 were previously reported and 10 are new predicted compounds for future synthetic investigations. Known crystal structures are labeled as ■, and predicted new structures as ♦. At the top of the plot, the fractions within each chemical system represent the number of predicted stable phases out of the total calculated.

2.3. Characterization. Laboratory XRD was measured on a Rigaku R-Axis Spider diffractometer using a Cu Kα source (λ = 1.54056 Å, 40 kV, 36 mA) in the Debye−Scherrer geometry outfitted with a curved image-plate detector. Powder XRD data for structure refinements were collected on a PANalytical Empyrean X-ray diffractometer with a Cu Kα X-ray source (λ_1 = 1.54056 Å, λ_2 = 1.544426 Å, 40 kV, 40 mA) in the Bragg−Brentano geometry on a spinning sample stage with a Si substrate. The step size was 0.0131 (2θ) with a 180 ms count time at each step. All Rietveld refinements were performed using the General Structure Analysis System-II (GSAS-II) software for extraction of crystallographic information.[27]

UV−vis diffuse reflectance spectroscopy (DRS) was measured using a Shimadzu UV−vis−NIR spectrophotometer (UV-3600) with an integrating sphere detector from 250 to 1000 nm. The sample was spread evenly and pressed onto a flat $BaSO_4$ (Sigma-Aldrich, 99%) surface which served as the background reference. The analyte reflectance was measured and transformed using the Kubelka−Munk Remission function and plotted as a Tauc plot versus $h\nu$.[28] The approximate direct and indirect band gaps were determined by linear interpolation of the transformed absorption band edges.[29] Second harmonic generation (SHG) spectra were recorded by using the Kurtz−Perry method with Q-switched Nd/YAG lasers at the wavelength of 1064 nm.[30] Polycrystalline samples of $BaLa_4Ti_4O_{15}$, $SnLa_4Ti_4O_{15}$, and KH_2PO_4 (KDP) were ground and sieved into a distinct particle size range of 90−125 μm. Sieved KDP powder was used as a reference. The intensity of the frequency-doubled output emitted from the sample was measured using a photomultiplier tube.

Scanning electron microscopy (SEM) and energy-dispersive spectroscopy (EDS) were performed using a JEOL SM 6010LA scanning electron microscope operating at an accelerating voltage of 20 kV equipped with a JEOL EDXS silicon drift detector. The surface compositions of the $BaLa_4Ti_4O_{15}$ and $SnLa_4Ti_4O_{15}$ samples were characterized using X-ray photoelectron spectroscopy (XPS) with an XPS/UVS-SPECS system featuring a PHOIBOS 150 analyzer under a pressure of approximately 3×10^{-10} mbar. The data were acquired using a Mg Kα X-ray source ($h\nu$ = 1253.6 eV), which operated at 10 kV and 30 mA (300 W). XPS spectra of the survey scan were recorded with a pass energy of 24 eV in a 0.5 eV step. The C 1s peak was used as an internal reference with a binding energy of 285 eV.

2.4. Photocatalysis Measurements. Photocatalysis reactions for OWS were adapted from a previous literature method.[31] In brief, core−shell $Rh_xCr_{2-x}O_3$ and CoO_x cocatalysts were photodeposited in situ by adding ∼100 mg of the $SnLa_4Ti_4O_{15}$ catalyst to a quartz photovessel with ∼40 mL of DI water. Solutions of $Na_3RhCl_6{\cdot}12H_2O$ (Beantown Chemical), K_2CrO_4 (Alfa Aesar, 99.0% min), and $Co(NO_3)_2{\cdot}6H_2O$ (Alfa Aesar, 97.7% min) were prepared and used at targeted cocatalyst loadings of 0.1, 0.05, and 0.05 wt % for Rh, Cr, and Co metals, respectively, to the amount of catalyst used. The suspension was irradiated by a Xe arc lamp (300 W) after each metal addition and photodeposition onto the surfaces. For the suspended particle photocatalysis, the same reaction vessel from the previous step was used and the solution was degassed under N_2 gas for 30 min before sealing. The vessel was placed in front of a PR160L Kessil LED lamp with a set wavelength for each test. Wavelengths used were 390, 467, and 525 nm. The amount of gas produced was determined by an SRI 310C gas chromatograph equipped with a thermal conductivity detector (GC-TCD). Gaseous aliquots (500 μL) were measured once every hour over 3 h. Calibration curves for H_2 and O_2 (2:1) mixtures were measured to calculate the rates of gas evolution. Apparent quantum yields (AQYs) for each gas were determined by eq 3 (below) as established in prior reports[31]

$$\mathrm{AQY}(\%) = \frac{n \times N(\mathrm{gas})}{N(\mathrm{photons})} \times 100 \tag{3}$$

where n = 2 for H_2 and n = 4 for O_2. All experiments were performed in triplicate to establish the activity and photocatalytic stability versus reaction time and wavelength.

3. RESULTS AND DISCUSSION

3.1. Thermodynamic Stabilities of Multinary Sn(II)-Oxides. Structural modeling of hypothetical Sn(II)-containing oxides was done by the replacement of the divalent cations of known ternary oxides obtained from the International Crystal Structure Database. The host structures for the Sn(II) cation were chosen based on the following selection criteria: (1) an experimentally verified crystal structure, with (2) an A-site consisting of Sr(II), Ba(II), or Pb(II) cations which have been shown to be potentially ion-exchangeable with the Sn(II) cation,[5,9,12−15] and (3) exclusion of metal cations potentially redox reactive with the Sn(II) cation, e.g., Mo(VI), Mn(IV), and Re(VII). These criteria resulted in the calculation of the total energies of 52 hypothetical Sn(II)-containing oxides, with their thermodynamic stabilities given in Table S1 in the Supporting Information. As an example, discussed below, the potential decomposition pathway of the layered perovskite $SnLa_4Ti_4O_{15}$ is represented by eqs 4 and 5

$$SnLa_4Ti_4O_{15} \rightarrow SnO + 2La_2O_3 + 4TiO_2$$
$$\Delta E_{\mathrm{rxn}} = +\ 99\ \mathrm{meV\ atom^{-1}} \tag{4}$$

https://doi.org/10.1021/acs.chemmater.4c00929
Chem. Mater. 2024, 36, 5753−5763

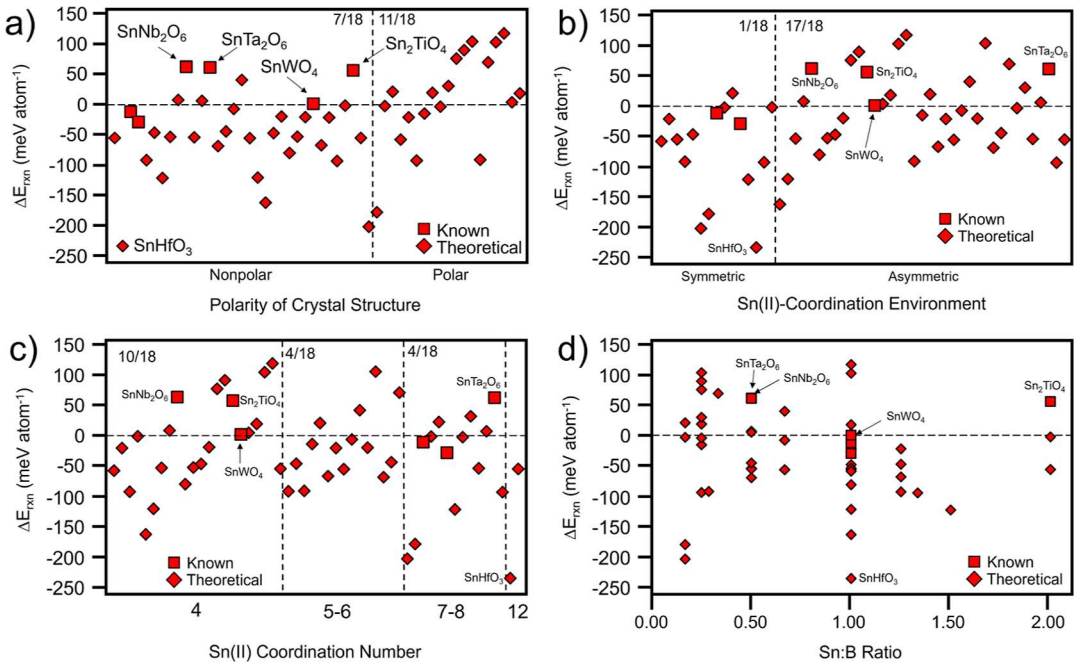

Figure 2. Plots of thermodynamic stability vs different structural parameters for the 52 Sn(II)-containing oxides, comparing the effects of (a) polar vs nonpolar space groups, (b) asymmetric versus symmetric local Sn(II)-coordination, (c) the Sn(II) coordination number, and (d) the Sn(II):B-site ratio (M = Ge, Hf, Nb, Ta, Ti, and W) in their structure. Known crystal structures are shown as ■, and theoretical structures as ♦. The fraction of stable phases in each bin is listed at the top of each plot.

$$2SnLa_4Ti_4O_{15} \rightarrow Sn_2TiO_4 + 4La_2O_3 + 7TiO_2$$
$$\Delta E_{rxn} = +\ 95\ \text{meV atom}^{-1} \quad (5)$$

where eq 4 represents the thermodynamic stability with respect to the binary oxides and eq 5 with respect to the known Sn_2TiO_4 ternary and binary oxides.

Figure 1a shows a summary of the relative thermodynamic stability for compounds in each of the chemical systems examined herein, with examples of stable and unstable structures drawn in Figure 1b. In this data set, 18 of the 52 computationally modeled Sn(II)-containing oxides were calculated to be stable with respect to currently known binary and ternary oxides, as arbitrarily sorted by B-site composition [e.g., Ti(IV), Ta(V), etc.]. The few previously reported ternary Sn(II)-containing oxides were included for internal comparisons and labeled, each of which was thermodynamically stable or fell within reasonable synthesizability limits (i.e., within 50−100 meV atom^{-1} of the convex hull). For example, α-$SnWO_4$ is calculated to be stable versus SnO and WO_3 (+0.15 meV atom^{-1}) and was first prepared by standard solid-state methods in air.[32] Conversely, the known $Sn_2Ta_2O_7$ pyrochlore is calculated to be unstable (−28.8 meV atom^{-1}) and requires stricter synthetic constraints.[33] One underlying question, though, is what structural factors control their relative thermodynamic stability? A molecular orbital approach described by the Revised Lone Pair model[34] proposes that cations with an ns^2 electron configuration [e.g., Sn(II), Pb(II), and Bi(III)] are stabilized in solids when the stereoactive lone pair is expressed, or as the crystal structure distorts to accommodate and minimize the electrostatic repulsions. For example, in romarchite SnO, layers of −O−Sn(II)−O− are bent as "zigzag" chains and allow the lone pair to project into interlayer cavities. Shown in Figure 1b are two example theoretical phases, $SnTi_4O_9$ and $SnHfO_3$. For $SnTi_4O_9$, results of calculations predict its structure to be stable versus SnO and TiO_2 by +85.4 meV atom^{-1}. By contrast, cubic $SnHfO_3$ is calculated to be unstable versus decomposition to SnO and HfO_2 by −226 meV atom^{-1}. Distinct differences between them include the lower-symmetry coordination environment for the Sn(II) cation in $SnTi_4O_9$ versus its regular cuboctahedral environment in $SnHfO_3$. From a steric perspective, this demonstrates the severe energetic penalty of not allowing the expression of the stereoactive lone pair of the Sn(II) cation. Furthermore, the Sn/Ti molar ratio is significantly lower than the Sn/Hf molar ratio (0.25 vs 1.0). The relationship between stability and Sn(II) concentration, which is described further below, can perhaps be understood more generally. Structures which host relatively greater amounts of Sn(II) cations would tend to suffer the largest energetic penalties. Despite these observations, $SnTi_4O_9$ has not been synthesized, while $SnHfO_3$ has been prepared with significant research efforts.[10] Thus, the calculated synthesizability of $SnTi_4O_9$, as well as nine other new phases, reveal promising synthetic targets for the rapid exploration of new Sn(II)-oxides.

In Figure 2a−d, the thermodynamic stabilities were plotted against various structural factors to gain a broader view and to reveal potential trends. In Figure 2a, it is shown that more than half of all the calculated unstable compounds occur with nonpolar space groups, while more than half (11/18) of the stable compounds are predicted with polar space groups. The nonpolar/polar nature of a crystal structure does not necessarily describe the coordination of the Sn(II) cation nor the expression of its stereoactive lone pair, locally. Figure 2b sorts the modeled Sn(II)-containing oxides by the occurrence of either asymmetric or symmetric Sn(II) coordination environments within their structures. Nearly all the stable phases (17/18) allow for lone pair expression within their crystal structures, like the $SnTi_4O_9$ structure described earlier in Figure 1b. Thus, while the stability of Sn(II)-oxides

https://doi.org/10.1021/acs.chemmater.4c00929
Chem. Mater. 2024, 36, 5753−5763

may be slightly influenced by an overall polar structure, the existence of local asymmetric coordination sites is a more predominant factor. Figure 2c shows that there is no clear trend when the same compounds are binned by the coordination number of the Sn(II) cation. More than half (10/18) of the stable structures have Sn(II) in a 4-fold coordination, as known in the ilmenite $SnTiO_3$ and Sn_2TiO_4 structures. Lastly, Figure 2d plots the Sn(II)/B-site ratio versus stability. All stable compounds except for Sn_2TiO_4 have a Sn/B molar ratio of ≤1, and more than half (11/18) have a molar ratio ≤0.5. To further probe this relationship, the cohesive energy versus the Sn/B ratio was plotted in Figure S1. With an increasing Sn(II) amount, the structures increasingly destabilize with less negative cohesive energies. A likely explanation is that the structure must "open up" to accommodate the space for the Sn(II) lone pair.

To summarize, 18 of the 52 theoretically modeled Sn(II)-containing oxides have been identified to be likely thermodynamically stable or borderline stable with respect to phase segregation to the constituent oxides, and 10 of these 18 have not yet been synthesized. The apparent trends reveal three predominating factors yielding enhanced thermodynamic stability, including (a) an asymmetric Sn(II) coordination environment, (b) a small Sn(II)/B molar ratio, and (c) a lower impact for polar space groups. A listing of the 10 new thermodynamically stable Sn(II)-containing oxides is given in Table 1. To confirm the synthesizability of the predicted

Table 1. List of 10 Theoretically Synthesizable Sn(II)-Containing Oxides Reported in This Work, Along with Their Predicted Structure Type, Space Group, and Energy Relative to the Convex Hull (ΔE_{hull})

composition	space group	structure type	ΔE_{hull} (meV/atom)
$SnNb_4O_{11}$	$P6_322$	tungsten bronze	−17.751
$SnTa_4O_{11}$	$P6_322$	tungsten bronze	−28.354
$Sn_2LaTa_3O_{11}$	$Immm$	Ruddlesden−Popper (n = 3)	−38.028
$Sn_5Ta_{10}O_{30}$	$P2$	tungsten bronze	−4.816
$SnTa_6O_{16}$	$Amm2$	tungsten bronze	−19.460
$SnLa_2Ti_3O_{10}$	$Ama2$	Ruddlesden−Popper (n = 3)	−66.050
$SnLa_4Ti_4O_{15}$	$P3c1$	(111)-layered perovskite	−99.040
$SnTi_4O_9$	$Pmmn$	$BaTi_4O_9$	−72.070
$SnLa_2WO_7$	$P2_1/c$	$BaLa_2WO_7$	−98.152
$SnLu_2WO_7$	$P2_1/c$	$BaLa_2WO_7$	−2.614

materials, the $SnLa_4Ti_4O_{15}$ layered perovskite was selected as a synthetic target owing to its fulfillment of each of the above conditions. Layered titanates have also previously been reported as promising ultraviolet-light photocatalysts for water splitting, as described further below.

3.2. Synthesis and Characterization of $MLa_4Ti_4O_{15}$ (M = Ba and Sn). The layered, hexagonal perovskite, $BaLa_4Ti_4O_{15}$ (BLTO), belonging to the $A_nB_{n-1}O_{3n}$ family of (111)-layered perovskites, was first prepared in high purity as a precursor to the predicted $SnLa_4Ti_4O_{15}$ compound with the same structure type. While the precise structure of BLTO is debated,[35,36] it has previously been reported to crystallize in either of the centrosymmetric space groups $P\bar{3}m1$ or $P\bar{3}c1$ or in the noncentrosymmetric and polar space group $P3c1$. The structure is composed of $La_2Ti_2O_7$ perovskite blocks separated by O−Ba−O layers along the (111)-plane. Symmetry determination has been challenging due to the difficulty of resolving Ba(II) and La(III) on similar crystallographic positions in the interlayer cavity because of their similar electron density and size. High temperature flux reactions within a molten $BaBr_2$ salt yielded BLTO crystals sufficiently large for single crystal XRD. Single-crystal data sets yielded possible structural solutions in the trigonal crystal system with lattice parameters of a = 5.5611(3) Å and c = 22.417(2) Å, and reflection conditions consistent with either the space groups $P3c1$ or $P\bar{3}c1$. SHG spectroscopy measurements on the BLTO powder gave a signal of ∼1.7× that of the KDP standard, shown in Figure S3, and therefore consistent with a noncentrosymmetric space group.[37] Subsequent structural refinements converged smoothly to R/R_w values of 0.022/0.052 in the space group $P3c1$, with a crystal structure closely consistent with previous reports of BLTO from powder XRD refinements. As a check of consistency, powder XRD data on the BLTO powder was also used to assess its purity and refined crystal structure of the bulk product. Rietveld refinements on the polycrystalline BLTO powder were consistent with the single crystal structure, yielding a wR_p = 5.99% and lattice parameters of a = 5.56796(9) Å and c = 22.4677(2) Å. A plot of the final Rietveld fitting is shown in Figure S2, and tables of select, refined parameter values and crystallographic data are reported in Tables S2−S6 in the Supporting Information.

The crystallites of BLTO formed as faceted hexagonal platelets ∼5 to 10 μm in diameter and ∼1 μm thick and confirmed to have the 1:4:4 stoichiometry using SEM and EDS measurements in Figures S4 and S5, consistent with the single crystal and powder XRD structure refinements. The BLTO crystallites were next reacted with a molar excess of a SnClF peritectic flux at 300 °C for 1 h under static vacuum to produce $SnLa_4Ti_4O_{15}$ (SLTO), as schematically represented in Figure 3a. The reaction is calculated to be thermodynamically driven by the large heat of formation of the BaClF salt side product upon Ba-for-Sn exchange ($\Delta H_f \approx -456$ kJ/mol),[38] as represented by eq 6 below

$$BaLa_4Ti_4O_{15} + SnClF \rightarrow SnLa_4Ti_4O_{15} + BaClF$$
$$\Delta E_{rxn} \approx -557 \text{ kJ mol}^{-1} \quad (6)$$

The SLTO product is predicted to be thermodynamically stable, implying a direct synthesis starting from SnO, TiO_2, and La_2O_3 is possible. However, the attempted solid-state reaction failed. As metal oxides typically require high temperatures to achieve sufficient interdiffusion, this is incompatible with the tendency for SnO to disproportionate under these conditions. Thus, the cation-exchange synthetic route allows the preformation of the desired substructure to facilitate a low-temperature pathway that circumnavigates the generally poor thermal stability of the Sn(II) cation. Intralayer ions have been generally observed to have much higher diffusion rates as compared to more condensed structures, allowing for a rapid Sn(II)/Ba(II)-diffusion through the interlayer spacing at relatively low temperatures.[39] The increased diffusion rates allow for the Sn(II) to selectively substitute for Ba(II) and retain the layered crystal structure and plate-like morphology. The SnClF and BaClF salts are both readily soluble in water and easily separated from the product.

The SLTO structure was characterized using high-resolution powder XRD data in the crystal structure with the polar space group $P3c1$, as described earlier. Full structure refinements of the XRD data showed that Sn had fully replaced Ba, with an

https://doi.org/10.1021/acs.chemmater.4c00929
Chem. Mater. 2024, 36, 5753−5763

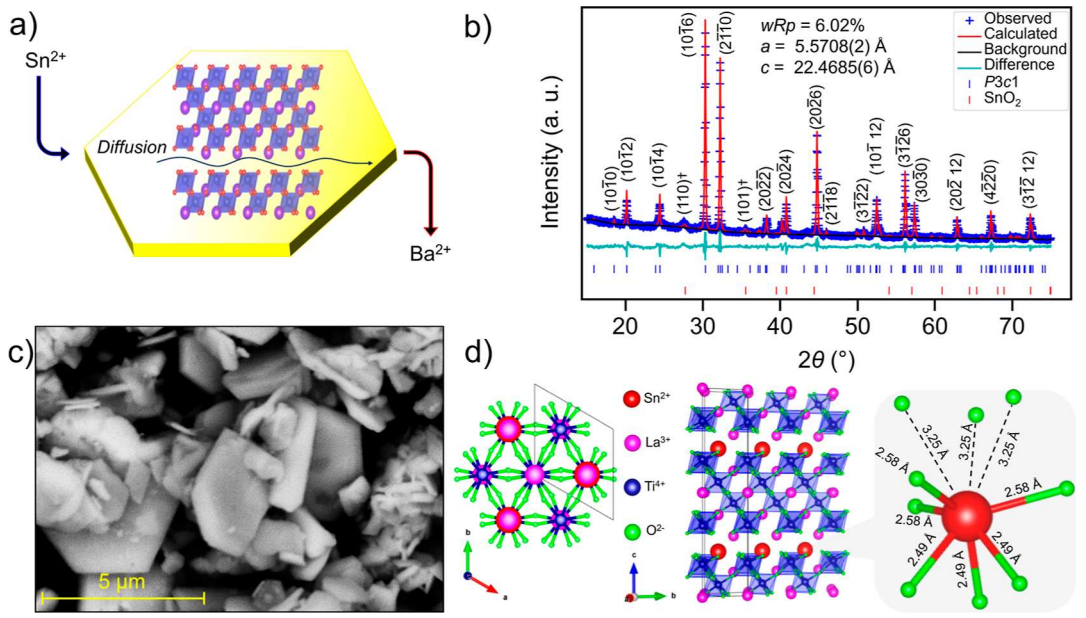

Figure 3. (a) Schematic representation of the synthesis of $SnLa_4Ti_4O_{15}$ by ion-exchange and (b) its final Rietveld refinement fitting in the space group *P*3*c*1 (no. 158) with secondary phase SnO_2 in the space group $P4_2/mnm$ (no. 136), (c) SEM image, and (d) polyhedral view of the crystal structure and local Sn(II)-coordination. Select peaks were indexed according to the hexagonal *P*3*c*1 setting and SnO_2 indices are denoted with a † for clarity. Predicted peak positions are noted by blue ticks for SLTO and red ticks for SnO_2. Atom types and interatomic Sn−O distances are labeled in (d).

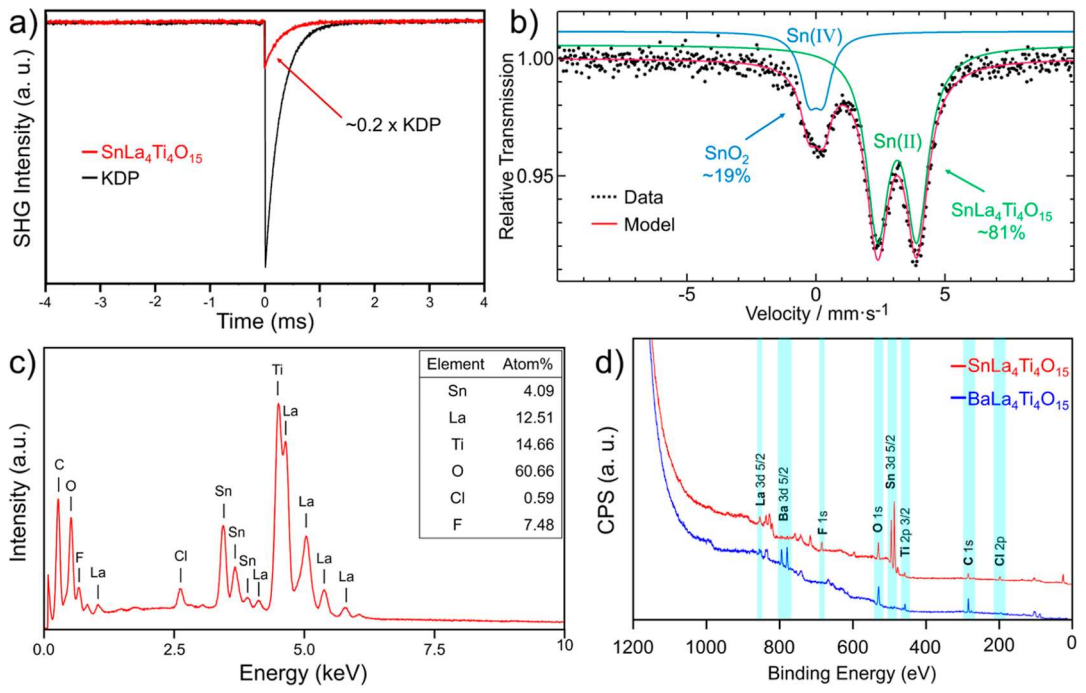

Figure 4. Experimental characterization data for $SnLa_4Ti_4O_{15}$ including (a) SHG activity versus a KDP standard, (b) ^{119}Sn Mössbauer spectrum at 78 K, (c) XPS data together with the $BaLa_4Ti_4O_{15}$ precursor, and (d) EDS data of chemical composition. Complete EDS data including elemental maps are included in the Supporting Information. Peaks used in XPS integration are highlighted in blue. For details, see the text.

occupancy of ∼100% for the Sn(II) cation. Shown in Figure 3b, the Rietveld refinement converged with a weighted residual of 6.0% and lattice parameters of a = 5.5708(2) Å, c = 22.4685(6) Å. Select refined parameter values are listed in Tables S5 and S7. Attempted structural refinements in the centrosymmetric setting yielded a poorer fit by comparison. The faceted plate-like morphology of the BLTO precursor was additionally maintained after Sn(II)-substitution in SLTO, as shown by SEM in Figure 3c. No significant change in particle size or shape was observed in the powder product. The crystal structure of SLTO, pictured in Figure 3d, can be described as consisting of layers of asymmetric O−Sn−O sheets and the expression of the Sn(II) lone pairs into the intralayer cavities. These perovskite layers comprised $La_2Ti_2O_7$-blocks terminating in the (111)-plane, a relatively uncommon feature in titanate-based perovskites.[40] Additionally, some SnO_2 impurity

https://doi.org/10.1021/acs.chemmater.4c00929
Chem. Mater. 2024, 36, 5753−5763

was observed by powder XRD and was corefined in the Rietveld analysis, as is consistent with surface oxidation as found commonly for Sn(II)-containing oxides. These results were further confirmed by additional characterization data, as discussed below, shown in Figure 4.

Figure 4a–d shows additional characterization data of the SLTO product. SHG measurements on SLTO, plotted in Figure 4a, also exhibited a nonlinear response with an intensity of ∼0.2× the signal of KDP at 1064 nm and consistent with the absence of an inversion center in the structure. We note that although the sample also contains the cassiterite-type SnO_2 in the space group $P4_2/mnm$ (no. 136), it is centrosymmetric and does not contribute to the SHG signal. The decrease in SHG intensity from 1.7× in BLTO to 0.2× KDP in SLTO after substitution is not immediately clear and will require additional investigations and is beyond the scope of this work. As shown in Figure 4b, the ^{119}Sn Mössbauer spectroscopy (78 K data) could be fit with the parameters listed in Table S9. The fitting of SLTO data shows Sn is primarily in the +2 oxidation state (∼81%), with a smaller amount of +4 (∼19%). The former corresponds to SLTO, while the latter can be explained by the presence of SnO_2 as noted earlier.

Shown in Figure 4c,d are the results of EDS and XPS characterization. The EDS data confirm the homogeneity and approximate stoichiometry of Sn–La–Ti (∼1:3:3) and no detectable Ba. The Sn is slightly more concentrated than the nominal stoichiometry due to the presence of the SnO_2 secondary phase. Generally, a few atomic percent of the chloride and fluoride anions were observed in some of the EDS spectra, close to the limit of detection, as a result of insufficient washing and removal of the salt flux at the surfaces. These amounts varied from sample to sample and decreased with additional washing steps, i.e., as found in comparing Figures S6 and S7 in the Supporting Information. The higher Cl/F concentrations in the XPS data (∼10 atom %), was also consistent with their location at the particles' surfaces. Surface corrosion by the SnClF flux is likely, as has been observed in similar reactions.[14] However, there was no detectable inclusion in the crystal structure, consistent with the full structure refinement of the powder XRD data. Contamination by Cl/F anions is not uncommon in halide-based flux reactions and requires follow-up studies of its impact on morphology and properties. The complex convolution of Ba, Ti, and La spectral peaks in the EDS spectra also necessitated the additional experimental check using XPS characterization data,[41] as plotted in Figures 4d and S8. Both the Sn and Ba $3d_{5/2}$ peaks have a substantial difference in binding energies (∼300 eV) which allow for their complete deconvolution, with quantitative results listed in Table S8.[42] Only Ba, La, Ti, O, and the C standard are detected in the BLTO powder, while the Sn(II)-exchange product of SLTO showed only Sn, La, Ti, O, Cl/F, and the C standard. It is important to note that the interaction volume of XPS hardly exceeds ∼10 to 30 nm into the sample surface. Therefore, the Sn-concentration is overestimated from the nominal 1:4:4 stoichiometry of Sn/La/Ti due to the formation of ∼10 nm thick SnO_2 shells on nearly all Sn(II)-containing materials.[43] The presence of Ba in levels as low as ∼0.1 atom % or smaller in the ground powder cannot be excluded based on the combined XPS and EDS results. More precise quantification will require further studies and perhaps nanoscale characterization.

To assess the thermodynamic stability of Sn(II)-containing SLTO, the powder was annealed under vacuum from 400 to 800 °C in 100 °C intervals. Its bulk purity and potential decomposition were checked at each interval using powder XRD, plotted in Figure 5. The most noticeable change

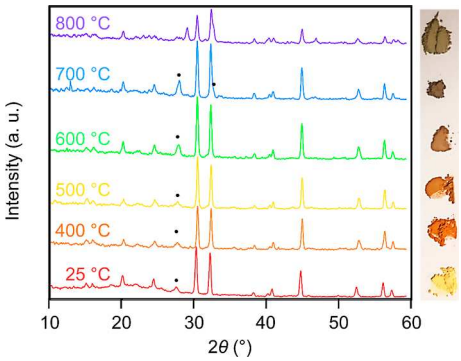

Figure 5. Ex situ room-temperature powder XRD data for $SnLa_4Ti_4O_{15}$ after heating to temperatures between 400 and 800 °C under static vacuum for 2 h with accompanying photographs of the product. The ● denotes peaks belonging to SnO_2 in the 25–700 °C plots.

observed upon heating was its color, which changed from yellow to orange beginning at ∼400 °C and then eventually to brown at 600–700 °C. By powder XRD, no significant change in the peaks matching with the layered perovskite structure is observed until 800 °C. At this temperature, the peaks for SLTO have both shifted slightly and become more amorphous and additional peaks are observed from new phases. The XRD peak at ∼27° (2θ) becomes more intense at 600–700 °C, which is consistent with the additional oxidation of Sn(II) into Sn(IV) and removal from the structure as cassiterite-SnO_2. The disappearance of SnO_2 at 800 °C and the emergence of new peaks suggests the Sn(IV) is participating in subsequent reactions and Sn(II) has been removed from the structure. Thus, the SLTO material shows significantly more thermal stability than previously reported Sn(II)-perovskites. For example, the recently reported $SnHfO_3$ decomposes into SnO and HfO_2 beginning at only ∼350 °C under vacuum.[14] However, SLTO retains its crystal structure even after annealing under vacuum at 700 °C. The color change is consistent with the disproportionation under vacuum of Sn(II) → Sn + Sn(IV) at the surfaces and material decomposition. Thus, the prediction-guided synthesis of a relatively more stable Sn(II)-oxide is confirmed for the SLTO phase.

3.3. Optical Properties and Calculated Electronic Structure. The formation of the new Sn(II)-exchanged SLTO from BLTO was found to occur with a color change of the polycrystalline powder from white to yellow. Measurements of the UV–vis DRS of the SLTO yielded direct and indirect band gap transitions of ∼2.8 and ∼2.4 eV, respectively, as plotted in Figure 6b. These values are significantly smaller as compared to the respective BLTO band gap transitions of ∼3.9 and ∼3.6 eV, Figures S9 and S10 and Table S10 in the Supporting Information. This redshift in the band gap of ∼1.2 eV into the visible-light wavelengths ($\lambda \leq$ ∼520 nm for SLTO) is consistent with the change in sample color and with prior reports of Sn-for-Ba exchange reactions.[9,10,15] To probe the origins of its smaller visible-light band gap, the electronic structure of SLTO was calculated for its geometry-relaxed

https://doi.org/10.1021/acs.chemmater.4c00929
Chem. Mater. 2024, 36, 5753–5763

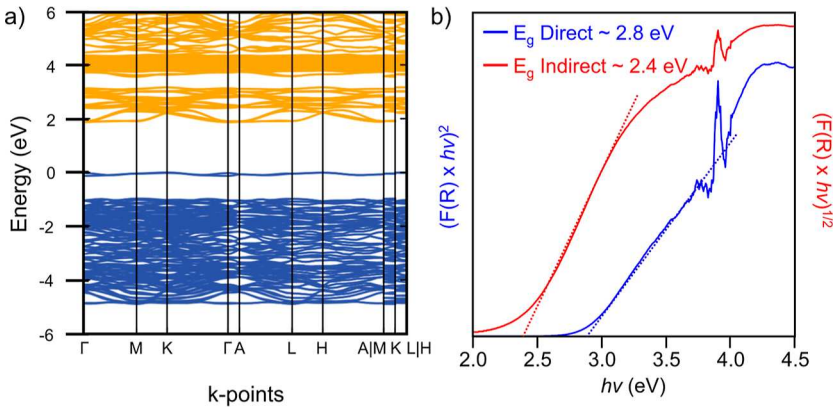

Figure 6. (a) Calculated band structure and (b) measured UV−vis diffuse reflectance data for $SnLa_4Ti_4O_{15}$. Extrapolated indirect and direct band gaps are labeled for the red and blue plots in (b).

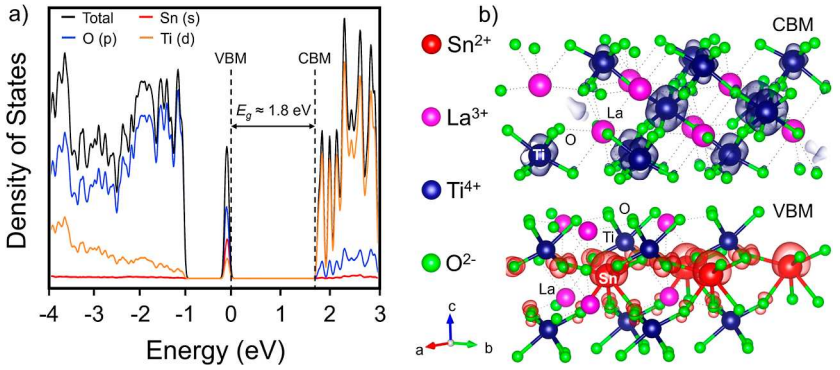

Figure 7. (a) Calculated DOS with the Fermi level set to 0 eV and (b) projected electron density for the CBM (top) and VBM (bottom) for $SnLa_4Ti_4O_{15}$. The La states are omitted from the plot for clarity and have no overlap with the frontier orbitals.

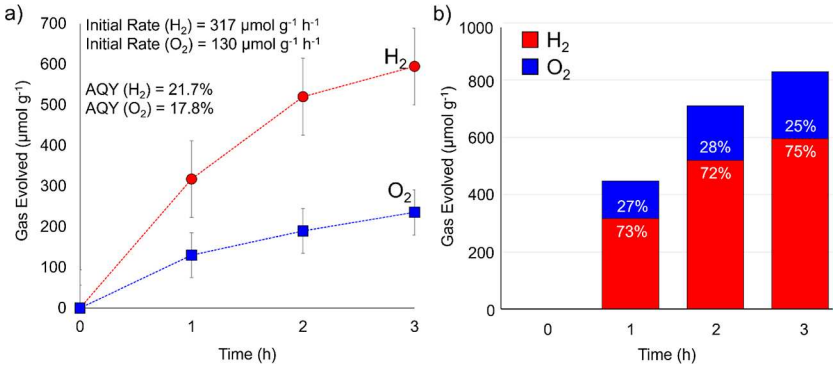

Figure 8. (a) Rates for OWS into H_2 and O_2 and (b) total evolved gas evolved, under 390 nm irradiation over 3 h reaction time. The surfaces of $SnLa_4Ti_4O_{15}$ were loaded with the Rh/Cr/Co cocatalysts in pure water.

crystal structure. Plots of the densities-of-states (DOS) and projected electron densities at the conduction and valence band edges are shown in Figure 7a. The valence band maximum (VBM) is composed of Sn(5s)-O(2p) filled states, while the conduction band minimum (CBM) is predominantly composed of empty Ti(3d) states. These results are consistent with other perovskites such as $BaTiO_3$.[44,45] The change from BLTO to SLTO is attributable to the addition of the Sn(5s) states within the band gap and increasing the VBM by ∼1.1 eV. Figure 7b shows the projected electron density of the CBM that is delocalized over the Ti−O layers. Conversely, the electron density at the VBM is localized over the O−Sn−O connectivity between the layers. The latter filled states occur at ∼1 eV above the O(2p) states. The stereoactive lone pair is formed by the hybridization of the Sn(5p) with the Sn(5s)−O(2p) antibonding orbitals, consistent with the revised lone pair model described earlier.[34] The addition of Sn(II) into the $SnLa_4Ti_4O_{15}$ structure thus shows a significantly decreased optical band gap as in recent reports of Sn(II)-substituted oxides.[5,9,14]

The calculated band structure of the atomic orbital contributions for SLTO is plotted in Figure 6a. With the addition of Sn(II), a relatively flat band appears just below the Fermi level and within the band gap. The absence of significant band dispersion stems from the isolated layer of Sn(II) cations with limited −O−Sn−O−Sn− connectivity. Additionally, the

https://doi.org/10.1021/acs.chemmater.4c00929
Chem. Mater. 2024, 36, 5753−5763

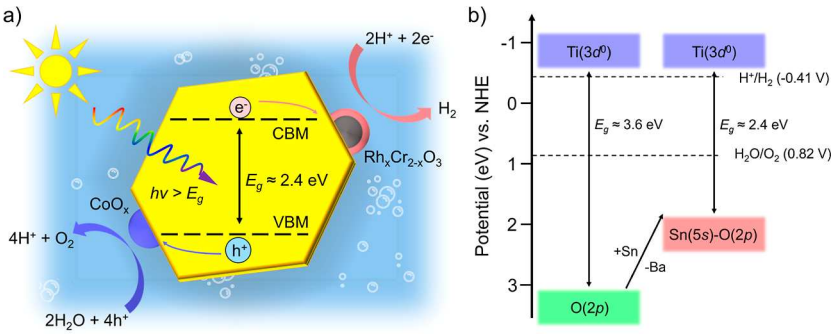

Figure 9. (a) Schematic of visible-light-driven OWS using the $SnLa_4Ti_4O_{15}$ photocatalyst and $Rh_xCr_{2-x}O_3/CoO_x$ surface cocatalysts, and (b) the valence and conduction band edge potentials vs NHE for $BaLa_4Ti_4O_{15}$ and $SnLa_4Ti_4O_{15}$.

calculated band gap of SLTO is ~1.8 eV, and which is ~0.6 eV smaller than the experimental band gap. This under-estimation of the band gaps of semiconductors is a well-documented problem of density functional theory calculations,[46] with the trends being more informative.

3.4. Suspended Particle OWS. Layered, hexagonal perovskites belonging to the $A_nB_{n-1}O_{3n}$ family, much like BLTO and SLTO, have been extensively demonstrated to be photocatalytically active for overall water splitting (OWS) with competitively high AQY of >10 to 20% under UV irradiation. Representative examples include the reported $Ba_5Nb_4O_{15}$,[47−49] as well as $BaLa_4Ti_4O_{15}$ described herein for the synthesis of $SnLa_4Ti_4O_{15}$.[40] The surface attachment of dual $Rh_xCr_{2-x}O_3/CoO_x$ cocatalysts is used to attain their high quantum efficiencies for stoichiometric OWS.[49] The deposited $Rh_xCr_{2-x}O_3$ and CoO_x cocatalysts improve charge-carrier separation at the surface, thereby reducing recombination and significantly increasing the rates of OWS. However, the large band gap of these layered perovskites remains a severe limitation that restricts their activity to UV light. Previous work has demonstrated that partial Sn(II)-substitution into $Ba_5Nb_4O_{15}$ can raise its valence band edge and represents an effective strategy for achieving water oxidation to molecular oxygen under visible light.[47] Thus, SLTO represents a promising candidate for visible-light-driven OWS.

The surfaces of the Sn(II)-exchanged SLTO powder were loaded with the $Rh_xCr_{2-x}O_3/CoO_x$ cocatalysts and testing for OWS under 390 nm irradiation in pure water. As shown in Figure 8a,b, ~594 μmol g^{-1} of H_2 are produced over 3 h with an initial rate of ~317 μmol g^{-1} h^{-1}, while ~235 μmol g^{-1} of O_2 are produced over 3 h with an initial rate of ~130 μmol g^{-1} h^{-1}. The AQYs of each gas were calculated using the initial rate of activity and found to be ~21.7% based on the H_2 yield and a slightly lower ~17.8% based on the O_2 yield. The approximate H_2:O_2 ratio was consistently ~2.3:1 across 3 h of irradiation, which is close to the nominal 2:1 stoichiometry. It should be noted that the GC detector had a lower sensitivity to O_2 and is one likely reason for the apparently higher H_2 production. Furthermore, the photocatalytic rates slow over time with the likely oxidative corrosion of Sn(II) at the surfaces and leading to the slight nonstoichiometric ratio. The overall initial rate was ~450 μmol g^{-1} h^{-1} and appeared to decrease over time to a maximum of ~283 μmol g^{-1} h^{-1} after 3 h. Without the surface cocatalyst, significantly smaller amounts of H_2 and O_2 were detected but were too low to quantify. At the longer wavelength of 467 nm, photocatalytic measurements showed the buildup of a consistent H_2/O_2 molar ratio and estimated to represent an initial H_2 evolution rate of ~96.2 μmol g^{-1} h^{-1} and AQY of ~5.2%. Under 525 nm light, the GC peak corresponding to H_2 was barely detectable. Because of the broad irradiance of the 525 nm LED source, most of the incident photons fall at lower energies than the band gap. The H_2/O_2 calibration data are shown in Figure S11 and qualitative summaries of the OWS activity under visible light are shown in Figure S12. After each photoreaction, SLTO retained its bulk structure, crystallinity, and morphology as shown by SEM and powder XRD data in Figures S13 and S14.

A schematic of the OWS mechanism and the approximate band edge energies of SLTO with respect to the water redox potentials are depicted in Figure 9a,b. The SLTO band edge energies are estimated based upon the known BLTO band edge energies and a red-shifted band gap after Sn(II)-exchange. With an increase in the valence band edge by ~1.1 eV in SLTO, both conduction and valence band edges are still compatible with OWS activity. Thus, these data demonstrate that the SLTO compound represents a promising new semiconductor for visible-light driven OWS owing to its more-optimal band edge energies and visible-light-absorbing band gap. It possesses a relatively flat valence band that is similar in nature to the known record-setting $BiVO_4$ water oxidation photocatalyst,[50] and which has required intense dopant studies to achieve a high mobility of charge carriers via a low-energy hopping mechanism. Future research is warranted in developing the full potential of SLTO for solar fuel applications.

4. CONCLUSIONS

The predictive modeling of hypothetical Sn(II)-containing oxides reveals underlying factors for increasing their thermodynamic stability. Potential host structures were identified that contain divalent cations, e.g., Ba(II) and Pb(II), that can be replaced by the Sn(II) cation. After replacement by Sn(II), total energy calculations on the geometry-relaxed structures show the highest stability for compositions (a) containing the Sn(II) cation in an asymmetric coordination environment and (b) with low Sn(II):B-site ratio. A total of 10 new Sn(II)-containing oxides are predicted to be stable versus the corresponding simpler binary and ternary oxides and are thus anticipated to be synthesizable. The significance of the modeling study is demonstrated by the targeted synthesis of one of these 10 phases, $SnLa_4Ti_4O_{15}$, which can be successfully prepared in high purity and crystallinity by a low temperature cation-exchange reaction. The $SnLa_4Ti_4O_{15}$ product is shown to crystallize in the polar and noncentrosymmetric space group $P3c1$ with a (111)-layered perovskite structure. The yellow powder exhibited a visible-light band gap of ~2.4 eV, with

https://doi.org/10.1021/acs.chemmater.4c00929
Chem. Mater. 2024, 36, 5753−5763

initial photocatalytic testing showing high AQY (~21.7% wrt H_2) for OWS over the course of 3 h. Future studies will further elucidate the photocatalytic performance and stability of $SnLa_4Ti_4O_{15}$. Additional work is motivated to more deeply probe the stability trends of complex Sn(II)-oxides with machine learning followed by synthetic efforts in the discovery of new Sn(II)-oxides. Thus, the applied hybrid approach of experimentally informed predictive modeling and subsequent targeted synthesis represents a promising strategy for overcoming severe synthetic bottlenecks in the attainment of new visible-light photocatalysts for solar energy conversion.

■ ASSOCIATED CONTENT

Supporting Information

The Supporting Information is available free of charge at https://pubs.acs.org/doi/10.1021/acs.chemmater.4c00929.

Results of density functional theory calculations for all theoretically modeled Sn(II)-containing multinary oxides, plots of the trends in compositions versus energies, crystallographic structural data with refinement plots and fitting parameters, SEM images with EDS spectra and maps, X-ray photoelectron and UV−vis DRS data, ^{119}Sn Mössbauer fitting parameters, plot of SHG, and gas chromatography data for the quantification of H_2 and O_2 from water-splitting photocatalysis experiments (PDF)

■ AUTHOR INFORMATION

Corresponding Author

Paul A. Maggard − *Department of Chemistry, North Carolina State University, Raleigh, North Carolina 27695-8204, United States;* orcid.org/0000-0002-3909-1590; Email: paul_maggard@ncsu.edu

Authors

Eric A. Gabilondo − *Department of Chemistry, North Carolina State University, Raleigh, North Carolina 27695-8204, United States*

Shaun O'Donnell − *Department of Chemistry, North Carolina State University, Raleigh, North Carolina 27695-8204, United States*

Subhendu Jana − *Department of Chemistry, North Carolina State University, Raleigh, North Carolina 27695-8204, United States*

Rachel Broughton − *Department of Materials Science and Engineering, North Carolina State University, Raleigh, North Carolina 27695-8204, United States*

Mingli Liang − *Department of Chemistry, University of Houston, Houston, Texas 77204-5003, United States*

Aylin Koldemir − *Institut für Anorganische und Analytische Chemie, Universität Münster, Münster 48149, Germany*

Jack Reichling − *Department of Chemistry, North Carolina State University, Raleigh, North Carolina 27695-8204, United States*

Carson Campbell − *Department of Chemistry, North Carolina State University, Raleigh, North Carolina 27695-8204, United States*

P. Shiv Halasyamani − *Department of Chemistry, University of Houston, Houston, Texas 77204-5003, United States;* orcid.org/0000-0003-1787-1040

Rainer Pöttgen − *Institut für Anorganische und Analytische Chemie, Universität Münster, Münster 48149, Germany*

Jacob L. Jones − *Department of Materials Science and Engineering, North Carolina State University, Raleigh, North Carolina 27695-8204, United States;* orcid.org/0000-0002-9182-0957

Complete contact information is available at: https://pubs.acs.org/10.1021/acs.chemmater.4c00929

Notes

The authors declare no competing financial interest.

■ ACKNOWLEDGMENTS

The authors acknowledge support of this work by the National Science Foundation (DMR-2004455). Additional components of this research were performed in part at the Analytical Instrumentation Facility (AIF) at North Carolina State University, which is supported by the State of North Carolina and the National Science Foundation (award ECCS-2025064). The AIF is a member of the North Carolina Research Triangle Nanotechnology Network (RTNN), a site in the National Nanotechnology Coordinated Infrastructure (NNCI). M.L. and P.S.H. thank the Welch Foundation (grant E-1457) and the NSF (DMR-2002319) for their support.

■ REFERENCES

(1) Matar, S. F.; Baraille, I.; Subramanian, M. A. First principles studies of $SnTiO_3$ perovskite as potential environmentally benign ferroelectric material. *Chem. Phys.* **2009**, *355* (1), 43−49.

(2) Taib, M. F. M.; Yaakob, M. K.; Badrudin, F. W.; Kudin, T. I. T.; Hassan, O. H.; Yahya, M. Z. A. First principles calculation of tetragonal (P4mm) Pb-free ferroelectric oxide of $SnTiO_3$. *Ferroelectrics* **2014**, *459* (1), 134−142.

(3) Wang, J.; Umezawa, N.; Hosono, H. Mixed valence tin oxides as novel van der Waals materials: theoretical predictions and potential applications. *Adv. Energy Mater.* **2015**, *6* (1), 1501190.

(4) Manikandan, M.; Tanabe, T.; Li, P.; Ueda, S.; Ramesh, G.; Kodiyath, R.; Wang, J.; Hara, T.; Dakshanamoorthy, A.; Ishihara, S.; Ariga, K.; Ye, J.; Umezawa, N.; Abe, H. Photocatalytic water splitting under visible light by mixed-valence Sn_3O_4. *ACS Appl. Mater. Interfaces* **2014**, *6* (6), 3790−3793.

(5) Hosogi, Y.; Kato, H.; Kudo, A. Photocatalytic activities of layered titanates and niobates ion-exchanged with Sn^{2+} under visible light irradiation. *J. Phys. Chem. C* **2008**, *112* (45), 17678−17682.

(6) Jiang, X.; Wang, M.; Luo, B.; Yang, Z.; Li, W.; Zhang, D.; Pu, X.; Cai, P. Magnetically recoverable flower-like $Sn_3O_4/SnFe_2O_4$ as a type-II heterojunction photocatalyst for efficient degradation of ciprofloxacin. *J. Alloys Compd.* **2022**, *926*, 166878.

(7) Sun, W.; Dacek, S.; Ong, S. P.; Hautier, G.; Jain, A.; Richards, W. D.; Gamst, A. C.; Persson, K. A.; Ceder, G. The thermodynamic scale of inorganic crystalline metastability. *Sci. Adv.* **2016**, *2* (11), No. e1600225.

(8) Campo, C. M.; Rodriguez, J. E.; Ramirez, A. E. Thermal behaviour of romarchite phase SnO in different atmospheres: a hypothesis about the phase transformation. *Heliyon* **2016**, *2*, No. e00112.

(9) O'Donnell, S.; Chung, C. C.; Carbone, A.; Broughton, R.; Jones, J. L.; Maggard, P. A. Pushing the limits of metastability in semiconducting perovskite oxides for visible-light-driven water oxidation. *Chem. Mater.* **2020**, *32* (7), 3054−3064.

(10) Gabilondo, E. A.; Newell, R. J.; Chestnut, J.; Weng, J.; Jones, J. L.; Maggard, P. A. Circumventing thermodynamics to synthesize highly metastable perovskites: nano eggshells of $SnHfO_3$. *Nanoscale Adv.* **2022**, *4*, 5320−5329.

(11) Gardner, J.; Thakre, A.; Kumar, A.; Scott, J. F. Tin titanate - the hunt for a new ferroelectric perovskite. *Rep. Prog. Phys.* **2019**, *82*, 092501.

(12) Diehl, L.; Bette, S.; Pielnhofer, F.; Betzler, S.; Moudrakovski, I.; Ozin, G. A.; Dinnebier, R.; Lotsch, B. V. Structure-directing Lone pairs: synthesis and structural characterization of $SnTiO_3$. *Chem. Mater.* **2018**, *30* (24), 8932−8938.
(13) Kumada, N.; Yonesaki, Y.; Takei, T.; Kinomura, N.; Wada, S. Preparation and crystal structure of a new tin titanate containing Sn^{2+}; Sn_2TiO_4. *Mater. Res. Bull.* **2009**, *44* (6), 1298−1300.
(14) Gabilondo, E. A.; Newell, R. J.; Broughton, R.; Koldemir, A.; Pöttgen, R.; Jones, J. L.; Maggard, P. A. Switching Lead for Tin in $PbHfO_3$: Noncubic Structure of $SnHfO_3$. *Angew. Chem., Int. Ed.* **2023**, *63*, No. e202312130.
(15) Gabilondo, E. A.; O'Donnell, S.; Broughton, R.; Jones, J. L.; Maggard, P. A. Synthesis and stability of Sn(II)-containing perovskites: $(Ba,Sn^{II})Hf^{IV}O_3$ versus $(Ba,Sn^{II})Sn^{IV}O_3$. *J. Solid State Chem.* **2021**, *302*, 122419.
(16) Tao, Q.; Xu, P.; Li, M.; Lu, W. Machine learning for perovskite materials design and discovery. *npj Comput. Mater.* **2021**, *7*, 23.
(17) Aykol, M.; Dwaraknath, S. S.; Sun, W.; Persson, K. A. Thermodynamic limit for synthesis of metastable inorganic materials. *Sci. Adv.* **2018**, *4* (4), No. eaaq0148.
(18) Lotfi, S.; Zhang, Z.; Viswanathan, G.; Fortenberry, K.; Mansouri Tehrani, A.; Brgoch, J. Targeting productive composition space through machine-learning-directed inorganic synthesis. *Matter* **2020**, *3*, 261−272.
(19) Oliynyk, A. O.; Mar, A. Discovery of intermetallic compounds from traditional to machine-learning approaches. *Acc. Chem. Res.* **2018**, *51* (1), 59−68.
(20) Tang, B.; Lu, Y.; Zhou, J.; Chouhan, T.; Wang, H.; Golani, P.; Xu, M.; Xu, Q.; Guan, C.; Liu, Z. Machine learning-guided synthesis of advanced inorganic materials. *Mater. Today* **2020**, *41*, 72−80.
(21) Bare, Z. J. L.; Morelock, R. J.; Musgrave, C. B. Dataset of theoretical multinary perovskite oxides. *Sci. Data* **2023**, *10*, 244.
(22) Zagorac, D.; Müller, H.; Ruehl, S.; Zagorac, J.; Rehme, S. Recent developments in the inorganic crystal structure database: Theoretical crystal structure data and related features. *J. Appl. Crystallogr.* **2019**, *52*, 918−925.
(23) Momma, K.; Izumi, F. VESTA 3 for three-dimensional visualization of crystal, volumetric and morphology data. *J. Appl. Crystallogr.* **2011**, *44*, 1272−1276.
(24) Kresse, G.; Hafner, J. Efficiency of Ab initio Total Energy Calculations for Metals and Semiconductors Using a Plane-Wave Basis Set. *Comput. Mater. Sci.* **1996**, *6*, 15−50.
(25) Kresse, G.; Furthmüller, J. Efficient Iterative Schemes for Ab initio Total-Energy Calculations Using a Plane-Wave Basis Set. *Phys. Rev. B: Condens. Matter Mater. Phys.* **1996**, *6*, 11169−11186.
(26) Perdew, J. P.; Burke, K.; Ernzerhof, M. Generalized Gradient Approximation made Simple. *Phys. Rev. Lett.* **1996**, *77*, 3865−3868.
(27) Toby, B. H.; Von Dreele, R. B. GSAS-II: the Genesis of a Modern Open-Source All Purpose Crystallography Software Package. *J. Appl. Crystallogr.* **2013**, *46* (2), 544−549.
(28) Simmons, E. L. Reflectance Spectroscopy: Application of the Kubelka-Munk Theory to the Rates of Photoprocesses of Powders. *Appl. Opt.* **1976**, *15*, 951−954.
(29) Morales, A. E.; Mora, E. S.; Pal, U. Use of Diffuse Reflectance Spectroscopy for Optical Characterization of Unsupported Nanostructures. *Rev. Mex. Fis.* **2007**, *53*, 18−22.
(30) Kurtz, S. K.; Perry, T. T. A Powder Technique for the Evaluation of Nonlinear Optical Materials. *J. Appl. Phys.* **1968**, *39*, 3798−3813.
(31) Takata, T.; Jiang, J.; Sakata, Y.; Nakabayashi, M.; Shibata, N.; Nandal, V.; Seki, K.; Hisatomi, T.; Domen, K. Photocatalytic water splitting with a quantum efficiency of almost unity. *Nature* **2020**, *581*, 411−414.
(32) Cho, I.-S.; Kwak, C. H.; Kim, D. W.; Lee, S.; Hong, K. S. Photophysical, photoelectrochemical, and photocatalytic properties of novel $SnWO_4$ oxide semiconductors with narrow band gaps. *J. Phys. Chem. C* **2009**, *113* (24), 10647−10653.
(33) Stewart, D. J.; Knop, O.; Meads, R. E.; Parker, W. G. Pyrochlores. IX. Partially oxidized $Sn_2Nb_2O_7$ and $Sn_2Ta_2O_7$: A Mössbauer study of Sn(II,IV) compounds. *Can. J. Chem.* **1973**, *51* (7), 1041−1049.
(34) Walsh, A.; Payne, D. J.; Egdell, R. G.; Watson, G. W. Stereochemistry of post-transition metal oxides: revision of the classical lone pair model. *Chem. Soc. Rev.* **2011**, *40*, 4455−4463.
(35) Zheng, H.; Woodward, D. I.; Gillie, L.; Reaney, I. M. Structure and microwave dielectric properties of $BaLa_4Ti_4O_{15}$. *J. Phys.: Condens. Matter* **2006**, *18*, 7051−7062.
(36) Harre, N.; Mercurio, D.; Trolliard, G.; Frit, B. Crystal structure of $BaLa_4Ti_4O_{15}$, member n = 5 of the homologous series $(Ba,La)_nTi_{n-1}O_{3n}$ of cation-deficient perovskite-related compounds. *Mater. Res. Bull.* **1998**, *33* (10), 1537−1548.
(37) Cammarata, A.; Zhang, W.; Halasyamani, P. S.; Rondinelli, J. M. Microscopic origins of optical second harmonic generation in noncentrosymmetric-nonpolar materials. *Chem. Mater.* **2014**, *26* (19), 5773−5781.
(38) O'Donnell, S.; Hamilton, A.; Maggard, P. A. Fast flux reaction approach for the preparation of Sn_2TiO_4: Tuning particle sizes and photocatalytic properties. *J. Electrochem. Soc.* **2019**, *166*, H3084−H3090.
(39) England, W. A.; Goodenough, J. B.; Wiseman, P. J. Ion-exchange reactions of mixed oxides. *J. Solid State Chem.* **1983**, *49*, 289−299.
(40) Miseki, Y.; Kato, H.; Kudo, A. Water splitting into H_2 and O_2 over niobate and titanate photocatalysts with (111) plane-type layered perovskite structure. *Energy Environ. Sci.* **2009**, *2*, 306−314.
(41) Newbury, D. E.; Ritchie, N. W. M. Is scanning electron microscopy/energy dispersive x-ray spectrometry (SEM/EDS) quantitative? *Scanning* **2012**, *35* (3), 141−168.
(42) Baer, D. R.; Artyushkova, K.; Cohen, H.; Easton, C. D.; Engelhard, M.; Gengenbach, T. R.; Greczynski, G.; Mack, P.; Morgan, D. J.; Roberts, A. XPS Guide: Charge neutralization and binding energy referencing for insulating samples. *J. Vac. Sci. Technol., A* **2020**, *38*, 031204.
(43) Diehl, L.; Fabini, D. H.; Vargas-Barbosa, N. M.; Jiménez-Solano, A.; Block, T.; Duppel, V.; Moudrakovski, I.; Küster, K.; Pöttgen, R.; Lotsch, B. V. Interplay between valence band tuning and redox stability in $SnTiO_3$: Implications for directed design of photocatalysts. *Chem. Mater.* **2021**, *33* (8), 2824−2836.
(44) Cohen, R. E.; Krakauer, H. Electronic structure studies of the differences in ferroelectric behavior of $BaTiO_3$ and $PbTiO_3$. *Ferroelectrics* **1992**, *136* (1), 65−83.
(45) Jain, A.; Ong, S. P.; Hautier, G.; Chen, W.; Richards, W.; Dacek, S.; Cholia, S.; Gunter, D.; Skinner, D.; Ceder, G.; Persson, K. A. Commentary: The materials project: A materials genome approach to accelerating materials innovation. *APL Mater.* **2013**, *1*, 011002.
(46) Perdew, J. P. Density Functional Theory and the Band Gap Problem. *Int. J. Quantum Chem.* **2009**, *28*, 497−523.
(47) O'Donnell, S.; Smith, A.; Carbone, A.; Maggard, P. A. Structure, stability, and photocatalytic activity of a layered perovskite niobate after flux-mediated Sn(II) exchange. *Inorg. Chem.* **2022**, *61* (9), 4062−4070.
(48) Yugo, M.; Hideki, K.; Kudo, A. Water splitting into H_2 and O_2 over $Ba_5Nb_4O_{15}$ photocatalysts with layered perovskite structure prepared by polymerizable complex method. *Chem. Lett.* **2006**, *35*, 1052.
(49) Kurashige, W.; Mori, Y.; Ozaki, S.; Kawachi, M.; Hossain, S.; Kawawaki, T.; Shearer, C.; Iwase, A.; Metha, G.; Yamazoe, S.; Kudo, A.; Negishi, Y. Activation of water-splitting photocatalysts by loading with ultrafine Rh-Cr mixed-oxide cocatalyst nanoparticles. *Angew. Chem., Int. Ed.* **2020**, *59* (18), 7076−7082.
(50) Wang, L.; Shi, X.; Jia, Y.; Cheng, H.; Wang, L.; Wang, Q. Recent advances in bismuth vanadate-based photocatalysts for photoelectrochemical water splitting. *Chin. Chem. Lett.* **2021**, *32* (6), 1869−1878.

https://doi.org/10.1021/acs.chemmater.4c00929
Chem. Mater. 2024, 36, 5753−5763